Integrating Newton's equations of motion in the reciprocal space

Antonio Cammarata,[1,a] (iD) Miljan Dašić,[1,2] (iD) and Paolo Nicolini[1,3,a] (iD)

AFFILIATIONS

[1] Department of Control Engineering, Faculty of Electrical Engineering, Czech Technical University in Prague, Technicka 2, 16627 Prague, Czech Republic

[2] Scientific Computing Laboratory, Center for the Study of Complex Systems, Institute of Physics Belgrade, University of Belgrade, Pregrevica 118, 11080 Belgrade, Serbia

[3] Institute of Physics (FZU), Czech Academy of Sciences, Na Slovance 2, 18200 Prague, Czech Republic

[a] Authors to whom correspondence should be addressed: cammaant@fel.cvut.cz and nicolini@fzu.cz

ABSTRACT

We here present the normal dynamics technique, which recasts the Newton's equations of motion in terms of phonon normal modes by exploiting a proper sampling of the reciprocal space. After introducing the theoretical background, we discuss how the reciprocal space sampling enables us to (i) obtain a computational speedup by selecting which and how many wave vectors of the Brillouin zone will be considered and (ii) account for distortions realized across large atomic distances without the use of large simulation cells. We implemented the approach into an open-source code, which we used to present three case studies: in the first one, we elucidate the general strategy for the sampling of the reciprocal space; in the second one, we illustrate the potential of the approach by studying the stabilization effect of temperature in α-uranium; and in the last one, we investigate the characterization of Raman spectra at different temperatures in MoS_2/MX_2 transition metal dichalcogenide heterostructures. Finally, we discuss how the procedure is general and can be used to simulate periodic, semiperiodic, and finite systems such as crystals, slabs, nanoclusters, or molecules.

Published under an exclusive license by AIP Publishing. https://doi.org/10.1063/5.0224108

I. INTRODUCTION

Molecular Dynamics (MD) simulation is the technique of choice to study a vast variety of atomic systems, spanning biological matter and inorganic materials.[1] In an MD simulation, interactions among a given set of atoms are defined by a function, i.e., the potential energy, which depends on the position of the atoms in the space; such interactions are provided as analytical functions or numerical datasets, which define the *force field*.[1] The vast majority of force fields rely on a classical description of interactions; in the past decades, several of them have been developed for both organic and inorganic systems.[2–7] Despite such an abundance of parameterizations, shortcomings of classical force fields are still present, e.g., in terms of accuracy and availability of the description for the system under study.[8–12] Moreover, the parameterization procedure presents an unavoidable degree of arbitrariness (for example, in the choice of the analytical form of the force field, or in the reference

data to be used, or even in the fitting scheme to be employed), as well as possibly being very time-demanding.[13,14] Another issue is represented by the difficulty of describing how the subtle details of the electronic density determine the force field, especially when the polarity of the bonds,[15] charge anisotropy,[16] and covalent character are decisive in the system dynamics.[17–19] On the other hand, one can perform *ab initio* molecular dynamics (AIMD)—such as in the Car–Parrinello scheme[20]—in order to overcome the abovementioned limitations imposed by classical force fields. In this case, the classical Hamiltonian is substituted by a quantum mechanical one, which can be built for any atom topology and atomic type. The major drawback of such schemes is that they might become very computationally demanding. Another possibility is represented by the QM/MM scheme,[21] where the system is split into two regions, one treated at the quantum mechanical (QM) level and the other (MM) at the classical one. Such an approach has the advantage that, in general, the simulations scale roughly as $O(N^2)$, where N is the

number of atoms in the system. However, the identification of the QM region requires *a priori* knowledge of the physical phenomena to be studied; moreover, the truncation of the bonds crossing the QM/MM interface is not trivial at all in, e.g., solid systems. Finally, in the QM/MM approach, a classical force field including all the chemical species of the system must be available.

In addition to this, large geometric models are often required in order to produce accurate data comparable with experiments,[22] resulting in resource-demanding MD simulations. The computational cost to produce a dynamical trajectory might become prohibitive if the simulations must be carried out at the quantum mechanical level. This issue is usually mitigated by limiting the size of the simulation box; however, it is known that this may affect the reliability of the results.[23] This is the case when it is necessary to include distortions realized across large interatomic distances, which account for ripples, and determine thermal transport, diffusion coefficients, and nucleation processes.[23–30]

Here, we propose an approach that can help circumvent these difficulties. The technique uses an approximation of the real potential energy surface by means of a Taylor expansion about a reference configuration, and it produces dynamical trajectories by solving Newton's equations of motion in terms of phonon normal coordinates. This, in turn, corresponds to a suitable sampling of the reciprocal space; such sampling enables the user to tune the computational load to target a desired accuracy. Moreover, long-wave structural modulations are accounted for with a suitable choice of sampling set, without the need to consider large unit cells. The general formulation of our approach enables us to parameterize the interatomic forces at any level of quantum mechanical description; such forces can be calculated from either ground or excited electronic configurations, even in the presence of external electric or magnetic fields, and may include quantum-mechanical electron–nuclei interactions such as the hyper-fine Hamiltonian. Since the atomic interactions appearing in the equations of motion can be parameterized with quantum mechanical descriptions, the sampling strategy of the technique makes it possible to generate dynamical trajectories of large systems on ordinary desktop computers. As the scheme is aimed at obtaining dynamical trajectories by integrating Newton's equations expressed in terms of normal coordinates, we termed it *Normal Dynamics* (ND).

In this work, we present the theoretical derivation of the method, the implementation into a freely available FORTRAN code, and advantages and drawbacks of this approach by considering three case studies. In the first one, we illustrate the general idea about how to perform the sampling of the reciprocal space, for example, by considering a reduced set of wave vectors of the Brillouin zone in order to obtain a computational speedup or by enlarging such a set in order to obtain the desired accuracy of the results. In the second one, we show that the ND scheme can be employed in order to observe the stabilization effect of temperature, which has been already reported in the literature,[31] but at the cost of performing computationally demanding AIMD simulations. In the third one, we exploit the ND technique to study the thermal effect in the Raman spectra of transition metal dichalcogenide heterostructures and discuss possible mistakes that may occur in the attribution of the Raman peaks.

II. THEORETICAL BACKGROUND

Differently from most of the classical force fields,[2–6] the ND technique does not rely on the definition of a bonding topology. It is rather based on a description that is general with respect to the atomic type and the geometric arrangement forming the system. Such a description relies on the Taylor expansion of the potential energy V in terms of the atomic displacements $\boldsymbol{u}$ with respect to a specified reference configuration,[32]

$$V(u_{i_k}^{\alpha_k}) = V_0 + \sum_{p \geq 1} \frac{1}{p!} \sum_{\substack{\alpha_1 \dots \alpha_p \\ i_1 \dots i_p}} \Theta_{i_1 \dots i_p}^{\alpha_1 \dots \alpha_p} \prod_{k=1}^{p} u_{i_k}^{\alpha_k}, \qquad (1)$$

where V_0 is the energy reference, p is the order of the terms in the sum, i_k and α_k identify the atom and the Cartesian component of the displacement from its reference position, respectively, and k enumerates the approximation orders. The Cartesian tensors $\boldsymbol{\Theta}_p = \Theta_{i_1 \dots i_p}^{\alpha_1 \dots \alpha_p}$ are formed by the pth order partial derivative of the potential energy with respect to the atomic positions calculated at the reference position. For $p = 1$, $\boldsymbol{\Theta}_1 = \Theta_{i_1}^{\alpha_1}$ is the net force active on the ith atom along the Cartesian direction α and is null when V is evaluated at equilibrium; for $p \geq 2$, $\boldsymbol{\Theta}_p$ contains the pth order interatomic force constants. If Eq. (1) is truncated at $p = 2$, the interatomic forces are of the harmonic kind; the anharmonic effects are instead included in the terms with $p \geq 3$. The $\boldsymbol{\Theta}_p$ tensors can be evaluated numerically at any order by means of a quantum mechanical Hamiltonian,[33–38] which avoids the limitations imposed by the availability of existing force fields or the need to parameterize a new one.[39] The use of a Taylor expansion to approximate the real potential energy surface is not new, and it is currently exploited in previous formulations[40] (also in different contexts[41]) and relative software packages, such as HIPHIVE,[34] A-TDEP,[31] and SSCHA.[42] The novelty of the ND method relies on the fact that we make use of the Fourier transform of such a Taylor expansion in order to explicitly perform dynamical simulations in the reciprocal space. To the best of our knowledge, this has never been proposed in the literature, and currently, there is no other software capable of performing such a task.

Equation (1) can be used to describe the atomic interactions of any system, irrespective of the atomic type, the stoichiometry, and the atom geometry. Moreover, the $\boldsymbol{\Theta}_p$ tensors represent harmonic ($p = 2$) and anharmonic ($p > 2$) contributions determined by the electronic density and the conditions at which the latter is calculated (e.g., ground or excited states, in the presence or not of external fields). However, it must be stressed that the technique relies on the Fourier transform of a Taylor expansion, which needs to be truncated for practical reasons, and therefore, it has a finite convergence radius. This results from the fact that the description of the interactions is somehow local, and it can become unreliable if the dynamics brings the system far away from the reference state, i.e., if large displacements take place during the dynamics. We address this point in Sec. III D, where we also present some strategies on how to (partially) amend this.

A. The equations of motion

Here, we present the equations employed by the ND scheme; the full derivation is reported in the supplementary material. We

26 August 2024 11:46:19

begin by exploiting the fact that, at each q wave vector of the Brillouin zone of a system with N atoms in the unit cell, the $3N$ normal coordinates Q_{qj} are a complete basis set for the $3N$ Cartesian components of the atomic displacements u_i^α. We shorten the notation as Q_λ, with $\lambda = (q, j)$ and j labeling the normal mode (for more details on the notation, see Sec. I of the supplementary material). The kinetic energy T and the potential energy V in terms of the Q_λ coordinates are then read as[32,43]

$$T = \frac{1}{2} \sum_\lambda \dot{Q}_\lambda \dot{Q}_\lambda^*, \tag{2}$$

$$V = \frac{1}{2} \sum_\lambda \omega_\lambda^2 Q_\lambda Q_\lambda^* + \sum_{p \geq 3} \frac{1}{p!} \sum_{\lambda_1 \ldots \lambda_p} \Phi_{\lambda_1 \ldots \lambda_p} \prod_{k=1}^{p} Q_{\lambda_k}, \tag{3}$$

where ω_λ is the eigenfrequency of the dynamical matrix associated with the phonon mode λ, the symbol "$*$" indicates the complex conjugation, p is the order of approximation, and the tensors $\Phi_p = \{\Phi_{\lambda_1 \ldots \lambda_p}\}$ are the Fourier transforms of the tensors Θ_p by means of the eigenvectors of the dynamical matrix.[32,43] We then write the Lagrangian of the system $\mathscr{L} = T - V$ by using Eqs. (2) and (3) and solving the Euler–Lagrange equations for the normal coordinates Q_λ,

$$\frac{d}{dt} \frac{\partial \mathscr{L}}{\partial \dot{Q}_\lambda} - \frac{\partial \mathscr{L}}{\partial Q_\lambda} = 0, \tag{4}$$

which are the Newton's equations of motion written in terms of the normal modes. The time integration of Eq. (4) represents the dynamic evolution of the normal modes of the system, and it is equivalent to the time integration of the Newton's equations of motion in Cartesian space. The explicit form of Eq. (4) is

$$\ddot{Q}_\lambda = -\omega_\lambda^2 Q_\lambda - \left(\sum_{p \geq 3} \frac{1}{(p-1)!} \sum_{\lambda_1 \ldots \lambda_{p-1}} \Phi_{\lambda \lambda_1 \ldots \lambda_{p-1}} \prod_{k=1}^{p-1} Q_{\lambda_k} \right)^*, \tag{5}$$

which shows that the atomic motion can be computed as a harmonic oscillation modulated by anharmonic contributions represented by the term in parenthesis, where p is the order of the anharmonic correction. If no anharmonic effects are present, that is, if all the Φ_p tensors are null, we recover the equation for the harmonic oscillator. The derivation of Eq. (5) and the calculation of harmonic phonons and anharmonic Φ_p tensors do not rely on the assumption that the reference unit cell represents a perfect crystal.

Indeed, the presence of defects can be taken into account by using a unit cell, which consists of a supercell containing the defect(s) and with a size that reproduces the desired defect concentration.

The choice of the q-points entering Eqs. (2) and (3) is done according to the kind of system that the cell represents, that is, periodic (bulk), semiperiodic (slab), or finite (cluster or molecule).

With the choice of the potential energy as shown in Eq. (3), Eq. (5) enables us to sample the phase space in the microcanonical ensemble (NVE). In order to simulate the canonical (NVT) ensemble within the ND scheme, Eqs. (2) and (3) must include the energy terms representing the degrees of freedom of a thermostat coupled with the system. We, therefore, derived the equations, which

include the Nosé–Hoover thermostat[44–46] (see Secs. II–IV of the supplementary material),

$$\ddot{Q}_\lambda = -\omega_\lambda^2 Q_\lambda - \left(\sum_{p \geq 3} \frac{1}{(p-1)!} \sum_{\lambda_1 \ldots \lambda_{p-1}} \Phi_{\lambda \lambda_1 \ldots \lambda_{p-1}} \prod_{k=1}^{p-1} Q_{\lambda_k} \right)^* - \dot{\xi} \dot{Q}_\lambda, \tag{6}$$

$$\ddot{\xi} = \frac{1}{Q_{th}} \left(\sum_\lambda \dot{Q}_\lambda \dot{Q}_\lambda^* - 3Nk_B T \right), \tag{7}$$

where ξ and Q_{th} are the dynamical variable and the "mass" associated with the thermostat, respectively, k_B is the Boltzmann's constant, and T is the set temperature. If ξ is constant during the whole simulation, Eq. (6) reduces to Eq. (5), and the simulated ensemble is the microcanonical one.

To the best of our knowledge, equations in the form of Eq. (5) or Eq. (6) have not been reported before, and we refer to them as *normal equations*.[47] In order to obtain the dynamical trajectory, the number of equations to be integrated is equal to the number of normal coordinates, that is, $3N \times N_q$, where N_q is the number of q points chosen to sample the Brillouin zone. The form of the normal equations provides a direct way to decompose the atomic motions into harmonic and anharmonic contributions, thus facilitating the study of anharmonic effects; indeed, the latter reduces to the study of the tensors Φ_p and how they determine the phonon scattering.[48–53]

We also developed FORTRAN software named *Phonon-Inspired Normal Dynamics Of Lattices* (PINDOL)[54] to simulate dynamical trajectories with the ND technique. At the moment, we implemented the harmonic and the first anharmonic term ($p = 3$); however, including higher orders is straightforward, and it will be done in future releases. We also plan to derive the normal equations to sample the phase space in the isobaric (NpT) ensemble in an upcoming work and implement them in a future version of the software. The equations that the PINDOL software solves are of the form

$$\ddot{Q}_\lambda = -\omega_\lambda^2 Q_\lambda - \left(\sum_{\lambda_1 \lambda_2} \Phi_{\lambda \lambda_1 \lambda_2} Q_{\lambda_1} Q_{\lambda_2} \right)^* \tag{8}$$

reproducing the microcanonical ensemble, or

$$\ddot{Q}_\lambda = -\omega_\lambda^2 Q_\lambda - \left(\sum_{\lambda_1 \lambda_2} \Phi_{\lambda \lambda_1 \lambda_2} Q_{\lambda_1} Q_{\lambda_2} \right)^* - \dot{\xi} \dot{Q}_\lambda \tag{9}$$

reproducing, together with Eq. (7), the canonical ensemble with the Nosé–Hoover thermostat.[44–46]

B. The q-point set

As it is apparent from the equations above, the essence of the normal dynamics technique is to recast Newton's equations in the reciprocal space by selecting a suitable set of q-points in the Brillouin zone. This results in several computational benefits.

One of the main advantages of the ND scheme can be appreciated by considering that, in order to describe distortions with long wavelengths in crystalline systems, one needs to simulate large unit cells, hence a large number of atoms. In fact, a standard molecular dynamics simulation can sample all and only the distortions that

26 August 2024 11:46:19

are commensurate with the simulation box; such distortions can be represented by the $3N$ phonon modes of the Γ point of the corresponding reciprocal lattice. In periodic systems, in order to capture the effect of long-range distortions, that is, to capture the effect of lattice distortions represented by waves with large wavelengths, we need to consider a suitable number, $N_r = N_a \times N_b \times N_c$, of replicas of the chosen unit cell; in this way, the number of equations of motion to be solved increases from $3N$ to $3N \times N_r$.

Let us consider a unit cell formed by N atoms and suppose that long-range structural modulations must be taken into account. We then create, for example, a $3 \times 3 \times 3$ supercell of the unit cell; the number of dynamical variables to be evolved in the Cartesian space is, therefore, $3N \times 3 \times 3 \times 3 = 81N$. In the case of the ND scheme (for more details, see Sec. V of the supplementary material), the number of dynamical variables in the *complete* set of *non-redundant* q-points is $42N$, which amounts to $(1 + 13 \times 2) \times 3N = 81N$ real variables, as for the Cartesian case, since the Q_{qj} are all complex quantities except for $q = (0, 0, 0)$. However, as we will show in the case studies, in principle, a similar result can be obtained by considering a *reduced* set of q-points (for example, by exploiting the symmetries of the unit cell). This immediately leads to a reduction of the degrees of freedom with respect to the Cartesian case, likely opening up a computational advantage.

Let us now imagine that, after an MD simulation, we realize that we need to further expand the size of our original $3 \times 3 \times 3$ system by considering, for example, a $6 \times 6 \times 6$ supercell; in this case, the number of dynamical variables increases from $81N$ to $648N$. In the ND scheme, instead, one can think of expanding the $\{q\}$ set by including suitable q-points only. For example, adding $q = (1/6, 1/6, 1/6)$ to the q_{333} set enables us to introduce atomic displacements that require a $6 \times 6 \times 6$ supercell to be represented in the real space; in this case, the number of variables increases from $81N$ to $81N + 6N = 87N$; that is, we reduced the number of dynamical variables by a factor of ~7. It is true that the vector $q = (1/6, 1/6, 1/6)$ alone does not fully represent a $6 \times 6 \times 6$ supercell, as the corresponding complete set would be made of 112 non-redundant q-points; however, we can incrementally include in our set more and more points of the kind q_{666} until we reach the desired accuracy.

The key point here is that ND simulations can be run *regardless of whether the $\{q_i\}$ set is complete or not*; the optimal size of the set is decided by the user according to the required accuracy. The ND sampling scheme then provides fine control over the computational load and of the accuracy the results. The number of dynamical (normal) variables increases as $O(N_q)$, where N_q is the number of q-points in the set; instead, in the standard Cartesian scheme, the number of variables increases as $O(L^3)$, where L is the number of replicas along one of the three directions. From this consideration and by keeping in mind that the scheme is essentially a coordinate transformation, it is clear that, in the case where one needs to consider the complete $\{q_i\}$ set, no computational speedup can be expected by using the ND technique. On the other hand, as we will show in Sec. III, in our case studies we do not need to consider a complete $\{q_i\}$ set to obtain a correct description of the relevant physical quantities, and we believe that this is likely to be the general case.

Another advantage of the ND scheme is that we can focus the computational load only on the relevant aspects of the dynamics. For example, let us imagine that only long waves traveling across

a $12 \times 12 \times 12$ supercell are relevant for our study and that the contributions from waves commensurate with a subset of the supercell could be neglected. In the Cartesian scheme, $3N \times 12 \times 12 \times 12 = 5184N$ variables must be somehow integrated, with no possibility of reducing such a number by neglecting unnecessary phonon contributions. On the contrary, in the ND scheme, it might be enough to consider, for example, just two wave vectors, $q_1 = (1/12, 1/12, 1/12)$ and $q_2 = (1/6, 1/6, 1/6)$, while neglecting all the other commensurate ones; in this case, we would need to integrate only $3N \times 2 \times 2 = 12N$ real variables ($N_q = 2$) instead of $5184N$.

III. RESULTS AND DISCUSSIONS

The goal of our case studies is to show that the ND scheme (i) is able to produce dynamical trajectories of large systems by using a common desktop computer and (ii) is capable of taking into account the effect of temperature, as is the case with standard Cartesian simulations. We extract the effective interatomic force constants[31,40,55–60] from ND runs at finite temperatures with the help of the HIPHIVE software;[34] we use the PHONOPY[61] and PHONO3PY[62] software for the necessary pre- and post-processing of the data. The steps to prepare, run, and analyze the simulations are reported in Sec. VI of the supplementary material.

The HIPHIVE software relies on a Taylor expansion of the forces on the atoms of the kind

$$F_i^\alpha = -\Theta_{ij}^{\alpha\beta} u_j^\beta - \frac{1}{2} \Theta_{ijk}^{\alpha\beta\gamma} u_j^\beta u_k^\gamma - \cdots , \qquad (10)$$

where F_i^α is the force on the ith atom along the Cartesian direction α evaluated as the negative gradient of the Taylor expansion of the potential energy V in Eq. (1).

The atomic displacements u and forces F are obtained from the normal coordinates Q and accelerations $\ddot{Q}$ calculated at each ND step and are supplied as an input to the HIPHIVE software; the latter performs a fitting of Eq. (10) and returns the effective interatomic force constants Θ at a finite temperature.

The first two case studies have been chosen to show how the method works as they have already been reported in the literature. The last case study, instead, has not been reported yet; indeed, we exploit the capabilities of the ND scheme to study the influence of temperature on the Raman spectrum of MoS_2/MX_2 bilayers and suggest how to properly characterize the Raman peaks.

To perform the simulations, the PINDOL code has been compiled with the GNU Cross Compiler v. 9.4.0 included in the software packages of the Ubuntu operative system version 20.04.5, Long Term Stable release. The trajectories have been produced on a local workstation equipped with an Intel Core i7-4770 CPU at 3.40 GHz; although we implemented a basic OpenMP parallelization, we did not use it for the present simulations.

The main quantities affecting the accuracy of an ND simulation are the Cartesian Θ_p tensors and the sampling of the reciprocal space: the first depends on the level of theory (i.e., classical or *ab initio*) and on the technical parameters used to evaluate the derivatives of the potential energy, while the latter is set by the user with the choice of the $\{q_i\}$ set. For example, the third order derivatives of the potential energy are the fundamental quantities determining the anharmonic effects at the first order. Their importance in determining the accuracy of the model has already

26 August 2024 11:46:19

TABLE I. Wall-clock time [hours and minutes] required by the ND simulations on crystalline silicon, α-uranium, and MoS$_2$/MX$_2$ systems at different samplings of the Brillouin zone ($N_{\boldsymbol{q}}$) and the number of unique non-null Φ_3 elements. The time shown is normalized to 4×10^6 dynamical steps and two atoms in the unit cell.

Case	Time	$N_{\boldsymbol{q}}$	#Φ_3
Si $\boldsymbol{q}_{333}$	8 h 10′	14	12 789
Si $\boldsymbol{q}_{555}$	69 h 39′	63	279 568
Si $\boldsymbol{q}_{555}^{red}$	1 h 53′	10	3 277
Si $\boldsymbol{q}_{666}^{red}$	4 h 6′	16	5 389
U $\boldsymbol{q}_{423}$	11 h 40′	14	38 059
U $\boldsymbol{q}_{423}^{red}$	7 h 30′	12	19 933
MoS/MX $\boldsymbol{q}_{441}$	96 h 10′	10	101 255
MoS/MX $\boldsymbol{q}_{441}^{red}$	1 h 25′	4	11 453

been discussed in previous computational studies;[63,64] in these, the authors also show that the use of a truncated Taylor expansion representing the potential energy abstracts the cost of a full AIMD when computing thermal conductivity. As for any computational model, the optimal simulation setup is the result of a compromise between the computational requirements and the accuracy of the produced data. The procedure to obtain an accurate evaluation of Θ_p is not the subject of the present discussion, as it does not depend on the ND framework; the reader can find information on the subject in any computational work that makes use of the Θ_p tensor (see Ref. 62 as an example). Instead, the choice of the $\{\boldsymbol{q}_i\}$ set is crucial to obtain reliable results from ND simulations.

In the present implementation of the ND technique within the PINDOL code, the computational load mainly depends on the number of elements in the Φ_3 tensor; such a number, in turn, depends on the number of $\boldsymbol{q}$-points considered, on the number of phonon modes per $\boldsymbol{q}$-point (i.e., $3N$), and on the components of the vectors forming the $\{\boldsymbol{q}_i\}$ set. In fact, only the phonon triplets $(\boldsymbol{q}, \boldsymbol{q}_1, \boldsymbol{q}_2)$ that satisfy the selection rule $\Delta(\boldsymbol{q} + \boldsymbol{q}_1 + \boldsymbol{q}_2) = 1$ are considered in the generation of the Φ_3 elements, as all the other triplets produce null elements.[32,43] In Table I, we report the simulation time for all the case studies that we consider; with $\boldsymbol{q}_{mnp}$, we indicate a complete $\{\boldsymbol{q}_i\}$ set formed by corresponding $N_{\boldsymbol{q}}$ $\boldsymbol{q}$-points, representing an $m \times n \times p$ supercell. The superscript "red" indicates that the set is formed by reducing the full sampling to only the irreducible $\boldsymbol{q}$-points; this has been obtained with the help of the SPGLIB library,[65] which is capable of exploiting the symmetries of the unit cell. We anticipate that, by inspecting Table I, in some cases, the use of a reduced set can drastically cut the computation time when compared with the full set case. For example, the time required to run the Si $\boldsymbol{q}_{555}$ case is reduced by 97% when the reduced $\boldsymbol{q}_{555}^{red}$ set is used, while in the case of the U and MoS$_2$/MX$_2$ systems, the time is reduced by 36% and 98%, respectively.

A. Convergence of the phonon dispersion with respect to the number of $\boldsymbol{q}$-points

As mentioned already, one of the main quantities governing the accuracy of the ND simulation is the sampling of the reciprocal space. In order to show this, we consider the Si crystal structure with the symmetries of the space group $Fd\bar{3}m$ (group number 227).

The starting geometry is the primitive unit cell with an optimized lattice parameter $a_p = 3.852$ Å, corresponding to the lattice parameter $a_c = 5.448$ Å of the conventional face centered cubic unit cell. The primitive cell contains only two Si atoms with reduced positions $(3/4, 3/4, 3/4)$ and $(1/2, 1/2, 1/2)$, respectively.

The interatomic forces are calculated within the density functional theory framework as implemented in the ABINIT software.[66–68] The Si atomic type is represented by a norm-conserving pseudopotential generated following the Troullier–Martins scheme[69] in the Kleinman–Bylander form,[70] considering four electrons in the valence shell and a cutoff radius of 2.1 Böhr, leading to a cutoff energy equal to 380 eV. Concerning the Self Consistent Field (SCF) parameters, we select the LDA Teter parameterization[71] as an energy functional, a $13 \times 13 \times 13$ Monkhorst–Pack mesh[72] to sample the Brillouin zone, and a plane wave cutoff equal to 500 eV; convergence is considered to be achieved when the difference in the total energy after three subsequent SCF cycles is below 3×10^{-10} eV. The starting atomic positions and lattice parameters are fully relaxed within a tolerance of 10^{-6} eV/Å; after relaxation, the structure preserves the initial cubic symmetry with a primitive (conventional) lattice parameter equal to 3.853 Å (5.445 Å), in good agreement with the experimental values.

In order to show how Brillouin zone sampling determines the accuracy of the ND simulations, we consider the harmonic phonon dispersion obtained from the finite displacements method[61] as our reference and compare it with the one calculated from the effective force constants extracted from the normal dynamics trajectory. To achieve this aim, the ND simulations are performed at different $\boldsymbol{q}$-samplings in the NVT ensemble with temperatures as low as 10 K in order to avoid anharmonic effects. Irrespective of the sampling, the maximum harmonic frequency is found to be $\nu_{max} \sim 11$ THz; according to the Nyquist–Shannon theorem, the time step can be $\Delta t = 1/(2\nu_{max}) \sim 23$ fs, but we reduce it to 1 fs as a safe value. The simulation window is 4 ns for a total of 4×10^6 dynamics steps. The time needed for each ND simulation is reported in Table I.

For the first ND simulation, we select a $3 \times 3 \times 3$ Monkhorst–Pack sampling, corresponding to the complete set $\boldsymbol{q}_{333}$ ($N_{\boldsymbol{q}_{333}} = 14$) representing a $3 \times 3 \times 3$ supercell. We observe that the phonon dispersion obtained from the effective force constants does not correctly reproduce the reference one (Fig. 1). We then increase the sampling of the reciprocal space by repeating the simulation with a $5 \times 5 \times 5$ mesh, corresponding to the complete set $\boldsymbol{q}_{555}$ ($N_{\boldsymbol{q}_{555}} = 63$); in this case, we obtain an improvement of the phonon dispersion. As a further test, we then perform the same simulation by using the set $\boldsymbol{q}_{555}^{red}$ ($N_{\boldsymbol{q}_{555}^{red}} = 10$), obtained by reducing the full $5 \times 5 \times 5$ mesh sampling to only the irreducible (and non-redundant) $\boldsymbol{q}$-points. In addition, in this case, we obtain a close agreement with the reference; this shows that similar accuracy can be reached via reciprocal space mesh sampling with reduced size. In this case, we used $2 \times 3 \times N_{\boldsymbol{q}_{555}^{red}} = 60$ dynamical variables, that is 5/7 and ~1/6 of the full $3 \times 3 \times 3$ and $5 \times 5 \times 5$ sampling, respectively ($2 \times 3 \times N_{\boldsymbol{q}_{333}} = 84$, $2 \times 3 \times N_{\boldsymbol{q}_{555}} = 378$). A further improvement has been obtained by considering the set $\boldsymbol{q}_{666}^{red}$ ($N_{\boldsymbol{q}_{666}^{red}} = 16$).

It is worth pointing out that, as described above, we could have proceeded in an alternative way. For example, we could have started from the set containing only the Γ and $(1/5, 1/5, 1/5)$ $\boldsymbol{q}$-points and
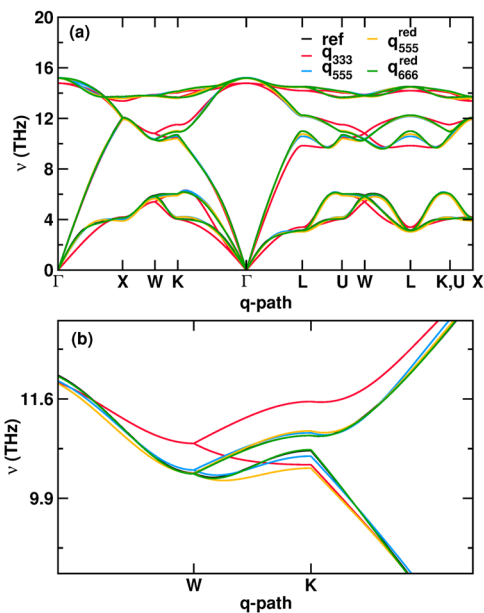
FIG. 1. (a) Phonon dispersion of crystalline silicon as obtained from the frozen phonon approach (ref) and extracted from the effective force constants at 10 K at different sampling sets. (b) Details of the phonon dispersion in (a). The best agreement is obtained for the q_{666}^{red} sampling; for this reason, the black line representing the reference dispersion is barely visible.

incrementally added further points until we reached agreement with the reference phonon dispersion. However, the irreducible q-point set contains high symmetry points, which are likely[73] to have a large role in the determination of the system dynamics. For this reason, and considering the little computation time, we decided to skip the incremental test and selected the mentioned $\{q\}$ sets as case examples. Such an approach also has the advantage that it does not require manual effort from the user thanks to the availability of libraries (e.g., SPGLIB[65]) that can automatically provide the list of the reduced set of q-points. Finally, it must be noted here that the accuracy of the phonon dispersion cannot be further improved when the sampling corresponds to supercells, including interatomic distances larger than the cutoff range used to calculate the force constants.

B. Stabilization of the optical Γ-Y branch in α-U

Let us now consider the case of α-uranium, where the effect of temperature is explicitly investigated. By lowering the temperature, uranium is known to undergo a phase transition at 50 K due to the softening of the longitudinal optical phonon mode in the [100] direction, involving the doubling of the unit cell.[74–77] In Ref. 31, this phenomenon has been studied by means of AIMD simulations performed by using hundreds to thousands of processors; here, we propose the same study carried out by means of ND simulations, each executed on one processor, and by using a computational setup equivalent to that adopted in the same published AIMD work. This shows that the ND approach enables one to perform the same study with reduced computational resources.

More in detail, we carried out ND simulations in the NVT ensemble at 50, 300, and 900 K, with a simulation window equal to 6 ns; the Brillouin zone sampling is performed by using the irreducible points of the $4 \times 2 \times 3$ Monkhorst–Pack mesh (q_{423}^{red} set), while the time step is set at 1 fs, being the maximum harmonic frequency equal to ~3.65 THz. In this case, we chose not to perform the convergence study as in the previous case, as here our main goal is to make a direct comparison with the results reported in Ref. 31. The lattice parameters and atomic positions of the reference structures are taken from experimental data at each considered temperature,[78–81] as has been done in previous simulations.[82] The interatomic forces are calculated within the density functional theory framework as implemented in the VASP software.[83–87] The plane wave energy cutoff is set to 435 eV, the k-mesh sampling to $2 \times 4 \times 2$ divisions according to the Monkhorst–Pack scheme, and the tolerance on the SCF convergence to 10^{-8} eV. The phonon and the third-order force constants have been calculated by using $4 \times 2 \times 3$ supercells of the conventional unit cell.

In Fig. 2, we report the phonon dispersion of the longitudinal optic-like phonon mode calculated by using the standard finite displacement approach, which does not take into account the effect of the temperature; in the same figure, for comparison, we report the phonon dispersion extracted from the ND simulations at the selected temperatures by calculating the corresponding effective interatomic force constants. The reference phonon dispersions [calculated with the finite displacement approach in Figs. 2(a)–2(c) and with DFPT in Figs. 2(d) and 2(e)] are evaluated at the experimental lattice parameters and atomic positions obtained at each temperature, as shown in Ref. 31. By comparing the dispersions at different temperatures, we observe that the ND simulations capture the hardening of the soft mode as the temperature increases, unlike the finite displacement approach [black line in Fig. 2, panels (a)–(c)]; this is expected because the phonon interaction is not taken into account in the latter method. We notice that the position of each dispersion minimum extracted from the ND simulations is slightly shifted with respect to the reference; we believe that this occurs for the following reason: The ND simulations are run using a primitive unit cell in order to exploit the computational advantages of the ND formalism; such a cell is obtained by means of the SPGLIB library,[65] which follows the convention of the Bilbao Crystallographic Server.[88,89] Our reference band dispersion is instead calculated by using the conventional unit cell as we think it is used in Ref. 31; in fact, we could not find enough computational details in Ref. 31, such as, for example, the specific settings (standard or arbitrary) and orientation of the unit cell used in the AIMD simulations. For this reason, we cannot determine the relative orientation between the conventional cell used for the reference and the primitive cell used for the ND simulations. We here recall that the components of the lattice parameters of the direct unit cell uniquely determine the components of the lattice parameters of the reciprocal unit cell, hence the coordinates of all the points of any path in the reciprocal space. Therefore, different direct lattice parameters generate different components of the points along the Γ-Y path and, as a consequence, a different position of the reference and ND-obtained dispersion minima. However, such a difference is small, and the experimentally observed hardening of the soft mode is reproduced by both ND and AIMD simulations. In addition, the quasi-harmonic approximation is not able to account for the frequency shift, while explicit temperature effects must be
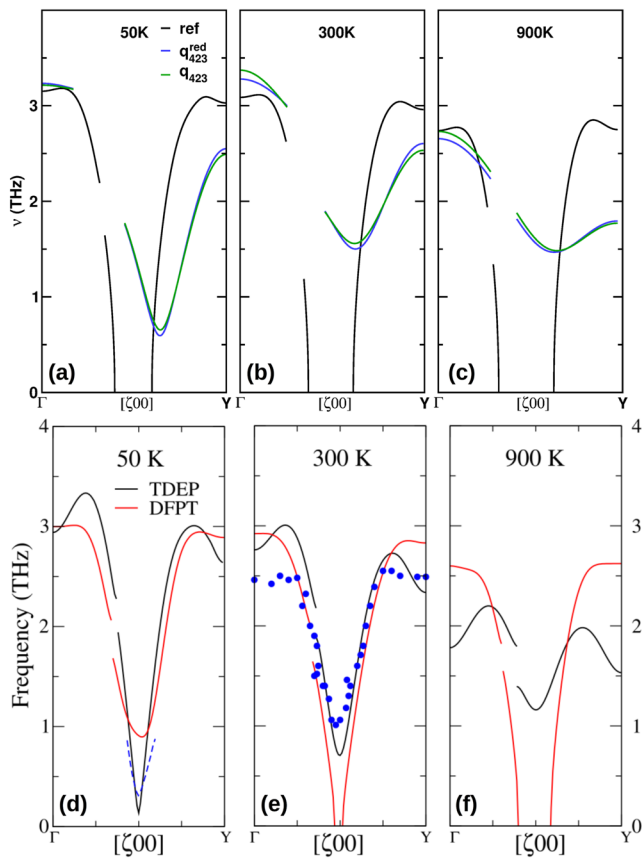
FIG. 2. Optic-like longitudinal branch of α-U at (a) 50 K, (b) 300 K, and (c) 900 K. The black, blue, and green lines represent the phonon dispersion obtained by the finite displacement approach and extracted from the ND simulations at the reduced (q_{423}^{red}) and full (q_{423}) sampling sets, respectively. Panels (d)–(f) are an adapted reproduction of Fig. 9 reported in Ref. 31 here reported for comparison; in such panels, black and red lines represent the results obtained by considering finite temperature effects explicitly and density functional perturbation theory, respectively. Experimental neutron-scattering data at 30 K[76] are denoted by a dashed line in panel (d) and at room temperature[75] by blue circles in panel (e), both here shown in the same way as in Ref. 31.

considered, as has been shown in the AIMD study, which we consider here for comparison.[31] The time needed to produce each ND trajectory is about 7 h 30′ (Table I) on a standard desktop computer (Sec. III). Finally, in order to show the computational benefits of working with a reduced set of q-points, we also performed the calculations using the complete set. One can notice that there is no appreciable difference in accuracy between the two calculations, while the computational speedup is about 36% (see Table I).

C. Raman shift in MoS$_2$/MX$_2$ bilayers

Heterostructures based on layered transition metal dichalcogenides (TMDs) find application in many fields, including photovoltaic devices, lithium-ion batteries, hydrogen evolution catalysis, desulfurization of fossil fuels, transistors, photodetectors, DNA detection, nanoelectromechanical systems, memory devices,

and tribology.[90–97] Research in these fields relies on local and non-invasive characterization methods capable of identifying the evolution of the physical properties with the number of layers and the temperature, assessing sample quality, and probing interlayer interactions; in this context, Raman spectroscopy is the technique of choice.[98] The positions of the Raman peaks depend on the Brillouin zone center phonons and their effective frequencies, as determined by phonon–phonon scattering processes; as a consequence, the positions depend on the temperature of the sample. Since the proper labeling of the Raman spectrum is central to the characterization of the material, the evolution of the peak position with temperature must be determined with adequate accuracy.

Transition metal dichalcogenides are layered structures with the general formula MX_2; each MX_2 layer is composed of a transition metal M atomic layer sandwiched between two chalcogen X atomic layers, while adjacent MX_2 layers are bound by weak van der Waals forces. In the present study, we consider bilayer heterostructures with M = Mo, W and X = S, Se. The space group symmetry of such systems is $P3m1$ (group number 156), with point group $3m$ (C_{3v} in Schöenflies notation[99]); accordingly, the active Raman modes own the character of the E and A representations.[100] The temperature effect on the E and A Raman peaks with the largest intensities has been studied experimentally mainly in MX_2 homostructures[101–105] and a few different heterostructures;[106–108] however, a full *ab initio* treatment is generally missing due to the highly demanding computational resources needed to run the supporting AIMD simulations. Here, we exploit the ND scheme to perform atom dynamics simulations with temperature values in the range [50, 500] K. Our references are the experimental 2H polymorph geometries of the MoS$_2$,[109] MoSe$_2$,[110] and WS$_2$[111] bulk systems. For each structure, we consider two subsequent MX_2 layers and set the length of the c crystallographic axes to 40 Å. We then substitute the Mo and S atoms in one layer with W and Se, respectively; in this way, we obtain the model geometries for the MoS$_2$/MoSe$_2$, MoS$_2$/WS$_2$, and MoS$_2$/WSe$_2$ bilayer heterostructures, which we name as MoS/MoSe, MoS/WS, and MoS/WSe, respectively (Fig. 3).

The optimized geometries and the interatomic forces are calculated within the density functional theory framework as implemented in the ABINIT software.[66–68] The plane wave energy cutoff is set to 500 eV and the Monkhorst–Pack k-mesh to $11 \times 11 \times 1$ divisions, while the tolerance on the SCF and the geometry convergence are set to 10^{-8} eV and 2.6×10^{-7} eV Å^{-1}, respectively. Following the results of previous studies,[112] we select the vdw-DFT-D3(BJ) correction[113] to account for the van der Waals interactions. The phonon spectrum and the third-order force constants have been calculated
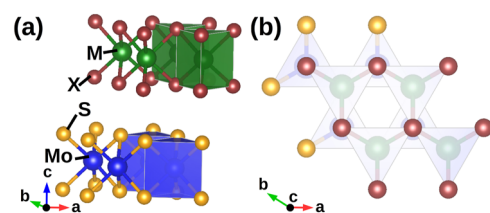

FIG. 3. (a) Lateral and (b) c-axis views of the model geometry of the trigonal P3m1 MoS/MX systems (M = Mo, W; X = S, Se).

by using $3 \times 3 \times 1$ supercells of the conventional unit cell. The effective force constants have been obtained from ND simulations in the NVT ensemble at 50, 100, 150, 200, 250, 300, 350, 400, 450, and 500 K by using the irreducible points of the $4 \times 4 \times 1$ Monkhorst–Pack mesh ($\boldsymbol{q}_{441}^{red}$ set); the simulation window is 4 ns, and it has been sampled with a time step equal to 1 fs. The corresponding Raman spectra have been obtained by means of the PHONOPY-SPECTROSCOPY tool,[114] which implements the formalism described in Ref. [115]. The intensity I of the Raman signal at a frequency ν and temperature T is calculated as

$$I(\nu, T) = \sum_{\lambda} \frac{I_0(\lambda)}{\pi} \frac{\frac{1}{2}\Gamma_\nu(\lambda, T)}{(\nu - \nu(\lambda))^2 + \left(\frac{1}{2}\Gamma_\nu(\lambda, T)\right)^2}, \quad (11)$$

where $I_0(\lambda)$ is the height of a delta function at the frequency $\nu = \nu(\lambda)$ of the Raman active mode λ obtained from the second order force constants, while the base intensity is spread over a range of frequencies due to the measurement uncertainty arising from the finite lifetime of the mode $\tau(\lambda, T) = \frac{1}{2\Gamma(\lambda,T)}$.

In turn, $\Gamma(\lambda, T)$ is calculated as

$$\Gamma(\lambda, \omega, T) = \frac{18\pi}{\hbar^2} \sum_{\lambda'\lambda''} |\Phi_{-\lambda\lambda'\lambda''}|^2$$
$$\times \left\{ [n(\lambda', T) + n(\lambda'', T) + 1]\delta[\omega - \omega(\lambda') - \omega(\lambda'')] \right.$$
$$+ [n(\lambda', T) - n(\lambda'', T)][\delta[\omega + \omega(\lambda') - \omega(\lambda'')]$$
$$\left. - \delta[\omega - \omega(\lambda') + \omega(\lambda'')]] \right\}, \quad (12)$$

where $\Phi_{\lambda'\lambda''}$ are the Fourier transforms of the third order force constants obtained at the temperature T, n is the occupation number of the mode λ at the temperature T calculated from the Bose–Einstein distribution, and $\omega = 2\pi\nu$.

The delta functions in Eq. (12) enforce the conservation of energy, and the mode linewidths $\Gamma(\lambda, T)$ are obtained by setting $\omega = \omega(\lambda)$.

The force constants that are fed into such formulations are extracted from each ND trajectory by means of the HIPHIVE software,[34] as described at the beginning of Sec. III.

The Raman active phonons are those belonging to the center of the Brillouin zone; therefore, only the phonons at $\boldsymbol{q} = \Gamma$ will be considered in our analysis. Irrespective of the system, all such phonons are Raman active; however, most Raman intensity concentrates in three intense peaks, two with the E character and one with the A character, which we label as E^1, E^2, and A, respectively. Each peak corresponds to a specific set of atom displacements, i.e., the phonon eigenvector, which identifies in a unique way the phonon responsible for a specific Raman transition (Fig. 4). It is, therefore, crucial to correctly characterize the eigendisplacements of the Raman active phonons in order to properly describe the layer interactions, track their evolution with any change in temperature, and compare their position across different chemical compositions.

We begin our analysis by taking the MoS/MoSe system as a reference. In order to find the corresponding E^1, E^2, and A peak positions in the MoS/WS and MoS/WSe systems, it is not enough to compare the eigenfrequency values and select the closest ones with the same character (i.e., E or A). In fact, at fixed character, the corresponding atom displacements might be different, despite the small difference between the two frequency values. Therefore, in
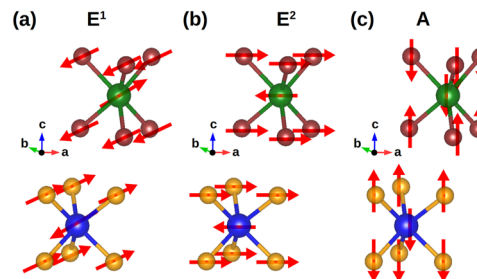

FIG. 4. Atom displacement patterns (red arrows) generating the most intense Raman peaks in the MoS/MX systems. The color code for the atoms is the same as in Fig. 3.

order to make a one-to-one correspondence among Raman peaks obtained at different temperatures and chemical compositions, we must identify the phonons with eigenvectors generating the same set of atom displacements. To achieve this aim, we can compare the eigendisplacements by direct inspection with suitable visualization software;[116,117] however, this is a non-rigorous and time-consuming approach. We choose instead to consider the scalar product between the real part of the phonon eigenvectors as a quantitative measure of the similarity between two sets of atomic displacements: the two sets are identical if the angle between the eigenvectors is null, while the smaller the angle, the more similar the displacement sets. In this way, we can systematically scan the eigenvectors of the MoS/WS and MoS/WSe systems and make a quantitative comparison with those of the reference (i.e., MoS/MoSe) generating the E^1, E^2, and A Raman peaks. We report the formalism in Sec. VII of the supplementary material, and implement it in the `eigmap` code.[118] The formalism is analogous to the one used in Ref. [119] to calculate the atom character of phonon eigenvectors. Following this phonon map procedure, we label the Raman peak positions of the three systems as shown in Fig. 5. We notice that the displacement pattern generating the A peak in MoS/WS does not correspond to the one generating the A peak in MoS/MoSe. This proves that a mapping procedure is actually needed in order to perform the correct peak attribution.

We now track the evolution of the modes with the temperature in each system. Let us recall here that the phonon modes are ordered
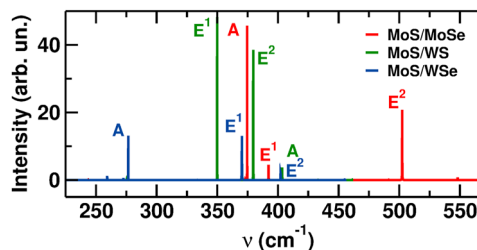

FIG. 5. Raman spectrum of the MoS/MX systems at 50 K. We focus the frequency range on the Raman signals with the largest intensity; the width of the peaks is not clearly visible due to the low temperature and the range of values chosen for the x-axis. The displacement pattern generating the A peak in MoS/WS does not correspond to the one generating the A peak in MoS/MoSe.
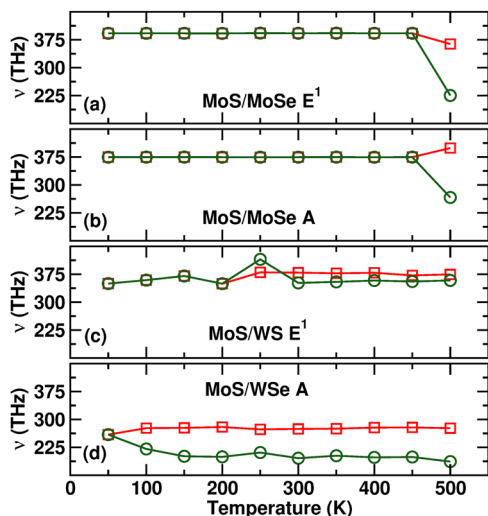
FIG. 6. Evolution of the Raman peaks of the systems with temperature. The right and wrong assignments are indicated by green and red symbols, respectively. Lines are a guide for the eye.

according to increasing eigenfrequencies and labeled with increasing integer numbers. Here, we would like to stress that, by increasing the temperature, the ordering of the modes can, in principle, change, and therefore, a mapping procedure is needed in order to perform a meaningful attribution. We first consider the MoS/MoSe system and focus on the peak E^1 at 392.35 cm^{-1} calculated at 450 K; this peak is labeled as $j = 12$. If we neglect the phonon mapping based on the atomic displacements and characterize the peaks only on the basis of the E symmetry and the difference between the frequencies, that peak would be considered shifted down to 363.54 cm^{-1} at 500 K [Fig. 6(a)]. Such a Raman signal is generated by the phonon mode $j = 15$. However, the displacement pattern of the two phonons is different. Instead, by means of the phonon mapping procedure discussed above, we understand that at 500 K, the E^1 peak is shifted down to 225.29 cm^{-1}, the latter generated by the mode $j = 9$ having the same eigendisplacement pattern as the mode $j = 12$ calculated at 450 K. This again shows that it is not enough to focus on a specific label of a phonon mode and track how its frequency changes at varying temperatures; at the same time, phonon labeling cannot be used to track the frequency of a phonon mode across different temperatures, as the label changes as the frequency of the phonon changes. Concerning peak A at 500 K, if the phonon displacement is not taken into account, a frequency of 399.42 cm^{-1} instead of 266.25 cm^{-1} would be assigned [Fig. 6(b)]. The abrupt drop of the E^1 and A frequencies going from 450 to 500 K is due to a sensitive softening of the corresponding phonon modes, indicating the possible appearance of structural instabilities at higher temperatures. Finally, in the MoS/WS and MoS/WSe systems, the erroneous attribution may occur already at 200 K [Fig. 6(c)] and 50 K [Fig. 6(d)], respectively.

The results show that a careful analysis of the phonon eigenvectors is essential for the correct assignment of the character of Raman peaks. This study has been feasible thanks to the ND scheme; in fact, it has made it possible to run dynamics simulations with a limited

amount of computational resources (Table I). As done for the previous case studies, we also performed the same calculations using the complete set of q-points. We recall that considering the complete set corresponds to perform dynamical simulations in the Cartesian space (i.e., the number of dynamical variables to be integrated is the same). In addition, in this case, it turned out that using a reduced set of q-points leads to a computational speedup, specifically of about 98% of the walltime. Finally, we would like to note that the scheme avoided the burden of parameterizing classical force fields, which are specific to the TMD chemical topology and composition considered in this case study.

D. Limitations of the ND approach

At the moment, being in their infancy, both the ND formulation and the PINDOL code show several limitations, which we plan to overcome as future developments of the present work.

The Cartesian tensors $\mathbf{\Theta}_p$, hence their Fourier transform $\mathbf{\Phi}_p$, representing the interatomic force constants, are evaluated by considering small atomic displacements from the reference position. However, during the dynamics, the atomic positions can change significantly, and, accordingly, the actual force constants might become very different from those provided as input to the simulation. This can be the case, for instance, of phase changes or diffusion of an adatom on a surface. In such scenarios, the computed normal forces may no longer be accurate. Moreover, the use of truncated polynomials as in Eq. (3) may produce unphysical saddle points in the potential energy landscape that lead to regions where the energy is not lower-bounded, with a possible divergence of the total energy during the dynamics.[120] In order to tackle this issue, perturbative approaches can be used.[121] Another possibility is the use of a multi-reference scheme. In fact, in cases where interrupting the dynamics and restarting it with a different reference configuration are not major issues, it is possible to foresee that a (possibly automatized) procedure of updating the $\mathbf{\Phi}_p$ tensors can be employed. For example, it is, in principle, possible to introduce a tolerance on the atomic displacements (set by the user at the beginning of the simulation), and if during the simulation the displacement of some atom becomes larger than the set tolerance, then the simulation is stopped. At this point, a new reference configuration can be created (such configuration may be built, e.g., by averaging the atom positions over a specified time window before the simulation stopped) and used as an input, together with the atomic positions and forces obtained in such a time window, for example, for the temperature dependent effective potential (TDEP) method[31] or the HIPHIVE code,[34] which will yield the updated force constants. Alternatively, the new reference configuration can be used to recalculate the phonons and the $\mathbf{\Phi}_p$ tensors with the same procedure used to prepare the input for the ND simulation. Both the tolerance on the atom displacements and the width of the time window can be chosen by the user. The former might be estimated from the variation of the total energy with respect to the starting configuration, while the latter should correspond to the last part of the trajectory where the interatomic distances are considered to be constant. At the moment, we have not implemented the tolerance check in PINDOL, but we plan to do it in future versions. At any rate, it must be stressed that even in cases where producing discontinuous dynamics is not an issue, if the potential energy surface of the system under study is very corrugated, that is, if it presents

a large number of local minima separated by low barriers (which is the case for, e.g., proteins[122]), then the benefits deriving from the exploitation of the ND scheme can be easily nullified by the need to frequently update the description based on the reference configuration. Nevertheless, we are confident that the proposed technique can be exploited for the investigation of a still large set of systems.

Moreover, when the phonon lifetimes are shorter than the Ioffe–Regel limit in time, it is no longer possible to describe phonon scattering in terms of the phonon wave vector q and index j, and the anharmonic effects here accounted for by the Φ_p tensors require a different formulation.[123] For this reason, the present ND formulation is valid whenever the Φ_p tensors are a good approximation of the anharmonic effects, the latter being the case of the majority of the simulation studies on lattice anharmonicity reported in the literature.

Concerning the PINDOL code, the amount of memory to store the Φ_3 tensor is minimized by exploiting its properties; the full tensor is reconstructed on the fly when evaluating the sum in Eq. (5), and the number of operations depends on the kind of triplet (see Sec. VI of the supplementary material). The computation time can then be reduced by a suitable parallelization of this step, which will be realized in the next version of the PINDOL code. At the moment, a simple OpenMP parallelization has been implemented but not used for the case studies discussed here. The size of the Φ_3 tensor can be further reduced by taking into account the phonon–phonon scattering selection rules involving the mode eigenvectors;[49] however, this feature is not yet implemented in the present version of PINDOL.

IV. CONCLUSIONS AND OUTLOOK

In this paper, we present the normal dynamics technique, introducing the theoretical background and showing its applicability in three case studies thanks to the open-source implementation that we developed.[54] These are some examples of the many possible uses of the proposed technique. In fact, normal dynamics simulations can produce dynamical trajectories that can be analyzed to calculate temperature- and pressure-dependent quantities, which are usually calculated with existing molecular dynamics techniques. With respect to these latter, among the advantages of the ND scheme, it is worth recalling that (i) we do not need to parameterize interatomic potentials specific to the system's chemical composition and topology and (ii) we can produce long dynamical trajectories of large systems on an ordinary desktop computer. The normal dynamics scheme also provides a straightforward decomposition of the atomic motions in terms of normal coordinates, thus facilitating the analysis of several phenomena such as heat transfer,[124–126] hydrodynamic phonon transport,[127] carrier transport,[128] thermoelectric effect,[129] and energy dissipation in tribological conditions.[48] The normal equations of motion can be modified in order to include atomic constraints or the presence of external forces that may simulate, for example, an external field exciting specific phonon modes[130,131] or dragging forces producing atomic drifts;[132,133] indeed, we plan to develop the corresponding equations and add such features in future versions of the PINDOL software. This approach can also pave the way for a novel route to study the entangled electronic and dynamic features. In fact, by calculating the Φ_p tensors for both the ground

and the excited state(s), it would be possible to run multiple parallel normal dynamics simulations coupled in a replica exchange fashion,[134] thus making it possible to investigate how electronic excited states determine the atom dynamics at a finite temperature. We finally note that the PINDOL software and the calculation of the Φ_p tensors can be interfaced with structure databases[135,136] and used in high-throughput calculations[137] for the discovery of new materials with target physical properties.

Standard molecular dynamics simulations require large unit cells in order to take into account long-range distortions. This results in a computational load that rapidly scales with the number of atoms; the situation is even worse if *ab initio* methods are to be used because of accuracy reasons and/or a lack of force fields. In these cases, the computational requirements might become unaffordable for the majority of researchers. The normal dynamics sampling scheme overcomes these difficulties. Since the equations of motion are integrated in the reciprocal space, a computational speedup can be obtained by a sensible selection of the considered $\{q\}$-points. In fact, optimal sampling can be achieved via the exploitation of the symmetries of the unit cell, a systematic increase in the $\{q\}$ set size, or any user-decided choice of the reciprocal points. The $\{q\}$ set determines the size of the simulated direct unit cell; each q-point of the kind $(1/m, 1/n, 1/p)$ represents an $m \times n \times p$ supercell by using only $6N$ instead of $3N \times m \times n \times p$ variables; this makes it possible to consider the effect of long-wave structural modulations at a limited computational load.

The sampling scheme of the normal dynamics technique implicitly includes periodic boundary conditions. The periodicity of the system is, in fact, accounted for by the use of the reciprocal space integration scheme, which is based on the concept of phonons. Nonetheless, the normal dynamics approach is also able to simulate semiperiodic or finite systems such as nanoclusters or molecules. Examples of semiperiodic systems are the MoS_2/MX_2 bilayers discussed in the last case study, for which we chose sets of the kind $\{(q_a, q_b, 0)\}$ in order to truncate the periodicity along the c axis. Finite (non-periodic) systems, instead, can be simulated by using only the Γ point, even though in this case the benefits coming from a custom selection of the reciprocal space are no longer in place.

Most of the computation time is spent for the evaluation of the sum in Eq. (8), appearing also in the NVT equations in Eq. (9), and depends on the number of $\Phi_{\lambda\lambda'\lambda''}$ elements; however, the latter is not directly proportional to the number of q-points in the set. In fact, the scattering rule $\Delta(q + q_1 + q_2) = 1$[32,43] excludes the $\{\lambda, \lambda_1, \lambda_2\}$ triplets that do not satisfy it and sets the corresponding $\Phi_{\lambda\lambda'\lambda''}$ elements to zero. This reduces the number of terms in the sum, but whether the rule is satisfied or not depends on the components of the points in the set. Another control of the computational load can then be obtained by selecting suitable q-points that limit the number of $\Phi_{\lambda\lambda'\lambda''}$ elements but also provide accurate results.

The results that we presented show that, in order to run long dynamical simulations on large systems, it is not always necessary to expand our computational capabilities (e.g., from standard to quantum computers); instead, as an alternative, it is better to focus on reducing the related computational demand, thus minimizing energy consumption, power costs, and technological effort. In this respect, the normal dynamics sampling scheme represents a tool to perform all-atom dynamical simulations on an ordinary

desktop computer, making the generation of dynamical trajectory calculations more and more accessible to a larger audience of researchers.

SUPPLEMENTARY MATERIAL

See the supplementary material for the detailed descriptions of the notation used (Sec. I), the derivation of the equations reported in the main text (Secs. II–IV), the partitioning of the q-point set (Sec. V), how to prepare, run, and post-process ND simulations (Sec. VI), and the mapping procedure described in the third case study (Sec. VII).

ACKNOWLEDGMENTS

AUTHOR DECLARATIONS

Conflict of Interest

The authors have no conflicts to disclose.

Author Contributions

Antonio Cammarata: Conceptualization (equal); Formal analysis (equal); Funding acquisition (equal); Investigation (equal); Methodology (equal); Software (equal); Writing – original draft (lead); Writing – review & editing (equal). **Miljan Dašić**: Formal analysis (equal); Investigation (equal); Methodology (equal); Software (equal); Writing – review & editing (equal). **Paolo Nicolini**: Conceptualization (equal); Formal analysis (equal); Funding acquisition (equal); Investigation (equal); Methodology (equal); Software (lead); Supervision (equal); Writing – review & editing (equal).

DATA AVAILABILITY

The PINDOL code presented in this paper is publicly available under open-source license at https://github.com/acammarat/pindol. The data that support the findings of this study are available from the corresponding authors upon reasonable request.

REFERENCES

[1] D. Frenkel and B. Smit, *Understanding Molecular Simulation: From Algorithms to Applications* (Academic Press, San Diego, CA, 1996).

[2] W. D. Cornell, P. Cieplak, C. I. Bayly, I. R. Gould, K. M. Merz, D. M. Ferguson, D. C. Spellmeyer, T. Fox, J. W. Caldwell, and P. A. Kollman, "A second generation force field for the simulation of proteins, nucleic acids, and organic molecules," J. Am. Chem. Soc. **117**, 5179–5197 (1995).

[3] W. L. Jorgensen and J. Tirado-Rives, "The OPLS [optimized potentials for liquid simulations] potential functions for proteins, energy minimizations for crystals of cyclic peptides and crambin," J. Am. Chem. Soc. **110**, 1657–1666 (1988).

[4] B. R. Brooks, R. E. Bruccoleri, B. D. Olafson, D. J. States, S. Swaminathan, and M. Karplus, "CHARMM: A program for macromolecular energy, minimization, and dynamics calculations," J. Comput. Chem. **4**, 187–217 (1983).

[5] W. R. P. Scott, P. H. Hünenberger, I. G. Tironi, A. E. Mark, S. R. Billeter, J. Fennen, A. E. Torda, T. Huber, P. Krüger, and W. F. van Gunsteren, "The GROMOS biomolecular simulation program package," J. Phys. Chem. A **103**, 3596–3607 (1999).

[6] A. K. Rappe, C. J. Casewit, K. S. Colwell, W. A. Goddard, and W. M. Skiff, "UFF, a full periodic table force field for molecular mechanics and molecular dynamics simulations," J. Am. Chem. Soc. **114**, 10024–10035 (1992).

[7] K. Chenoweth, A. C. T. van Duin, and W. A. Goddard, "ReaxFF reactive force field for molecular dynamics simulations of hydrocarbon oxidation," J. Phys. Chem. A **112**, 1040–1053 (2008).

[8] J. Wildman, P. Repiščák, M. J. Paterson, and I. Galbraith, "General force-field parametrization scheme for molecular dynamics simulations of conjugated materials in solution," J. Chem. Theory Comput. **12**, 3813–3824 (2016).

[9] D. Dubbeldam, K. S. Walton, T. J. H. Vlugt, and S. Calero, "Design, parameterization, and implementation of atomic force fields for adsorption in nanoporous materials," Adv. Theory Simul. **2**, 1900135 (2019).

[10] J. A. Harrison, J. D. Schall, S. Maskey, P. T. Mikulski, M. T. Knippenberg, and B. H. Morrow, "Review of force fields and intermolecular potentials used in atomistic computational materials research," Appl. Phys. Rev. **5**, 031104 (2018).

[11] D. Dubbeldam, S. Calero, T. J. H. Vlugt, R. Krishna, T. L. M. Maesen, E. Beerdsen, and B. Smit, "Force field parametrization through fitting on inflection points in isotherms," Phys. Rev. Lett. **93**, 088302 (2004).

[12] R. M. Betz and R. C. Walker, "Paramfit: Automated optimization of force field parameters for molecular dynamics simulations," J. Comput. Chem. **36**, 79–87 (2015).

[13] L.-P. Wang and T. Van Voorhis, "Communication: Hybrid ensembles for improved force matching," J. Chem. Phys. **133**, 231101 (2010).

[14] W. Ouyang, O. Hod, and R. Guerra, "Registry-dependent potential for interfaces of gold with graphitic systems," J. Chem. Theory Comput. **17**, 7215–7223 (2021).

[15] H. Heinz and U. W. Suter, "Atomic charges for classical simulations of polar systems," J. Phys. Chem. B **108**, 18341–18352 (2004).

[16] C. Kramer, A. Spinn, and K. Liedl, "Charge anisotropy: Where atomic multipoles matter most," J. Chem. Theory Comput. **10**, 4488–4496 (2014).

[17] A. L. Lomize, M. Y. Reibarkh, and I. D. Pogozheva, "Interatomic potentials and solvation parameters from protein engineering data for buried residues," Protein Sci. **11**, 1984–2000 (2002).

[18] A. Warshel, P. K. Sharma, M. Kato, and W. W. Parson, "Modeling electrostatic effects in proteins," Biochim. Biophys. Acta, Proteins Proteomics **1764**, 1647–1676 (2006).

[19] J. N. Israelachvili, *Intermolecular and Surface Forces* (Elsevier, San Diego, CA, 2011).

[20] R. Car and M. Parrinello, "Unified approach for molecular dynamics and density-functional theory," Phys. Rev. Lett. **55**, 2471–2474 (1985).

[21] A. Warshel and M. Levitt, "Theoretical studies of enzymic reactions: Dielectric, electrostatic and steric stabilization of the carbonium ion in the reaction of lysozyme," J. Mol. Biol. **103**, 227–249 (1976).

[22] R. Elber, "Perspective: Computer simulations of long time dynamics," J. Chem. Phys. **144**, 060901 (2016).

[23] F. Grasselli, "Investigating finite-size effects in molecular dynamics simulations of ion diffusion, heat transport, and thermal motion in superionic materials," J. Chem. Phys. **156**, 134705 (2022).

[24]Y. Hu, J. Chen, and B. Wang, "On the intrinsic ripples and negative thermal expansion of graphene," Carbon **95**, 239–249 (2015).

[25]U. Monteverde, J. Pal, M. A. Migliorato, M. Missous, U. Bangert, R. Zan, R. Kashtiban, and D. Powell, "Under pressure: Control of strain, phonons and bandgap opening in rippled graphene," Carbon **91**, 266–274 (2015).

[26]B. Smith, L. Lindsay, J. Kim, E. Ou, R. Huang, and L. Shi, "Phonon interaction with ripples and defects in thin layered molybdenum disulfide," Appl. Phys. Lett. **114**, 221902 (2019).

[27]X. Gu, Y. Wei, X. Yin, B. Li, and R. Yang, "Colloquium: Phononic thermal properties of two-dimensional materials," Rev. Mod. Phys. **90**, 041002 (2018).

[28]A. Mahata and M. Asle Zaeem, "Size effect in molecular dynamics simulation of nucleation process during solidification of pure metals: Investigating modified embedded atom method interatomic potentials," Modell. Simul. Mater. Sci. Eng. **27**, 085015 (2019).

[29]S. H. Jamali, L. Wolff, T. M. Becker, A. Bardow, T. J. H. Vlugt, and O. A. Moultos, "Finite-size effects of binary mutual diffusion coefficients from molecular dynamics," J. Chem. Theory Comput. **14**, 2667–2677 (2018).

[30]S.-F. Tsay and C. F. Liu, "System-size effects in the molecular-dynamics simulation of metallic crystallization," Phys. Lett. A **192**, 374–378 (1994).

[31]F. Bottin, J. Bieder, and J. Bouchet, "a-TDEP: Temperature dependent effective potential for abinit—Lattice dynamic properties including anharmonicity," Comput. Phys. Commun. **254**, 107301 (2020).

[32]D. M. Wallace, *Thermodynamics of Crystals* (John Wiley & Sons, Inc, 1972).

[33]S. Baroni, S. de Gironcoli, A. Dal Corso, and P. Giannozzi, "Phonons and related crystal properties from density-functional perturbation theory," Rev. Mod. Phys. **73**, 515–562 (2001).

[34]F. Eriksson, E. Fransson, and P. Erhart, "The hiphive package for the extraction of high-order force constants by machine learning," Adv. Theory Simul. **2**, 1800184 (2019).

[35]L. Chaput, A. Togo, I. Tanaka, and G. Hug, "Phonon-phonon interactions in transition metals," Phys. Rev. B **84**, 094302 (2011).

[36]K. Parlinski, Z. Q. Li, and Y. Kawazoe, "First-principles determination of the soft mode in cubic ZrO_2," Phys. Rev. Lett. **78**, 4063–4066 (1997).

[37]L. Paulatto, F. Mauri, and M. Lazzeri, "Anharmonic properties from a generalized third-order *ab initio* approach: Theory and applications to graphite and graphene," Phys. Rev. B **87**, 214303 (2013).

[38]X. Gonze and J.-P. Vigneron, "Density-functional approach to nonlinear-response coefficients of solids," Phys. Rev. B **39**, 13120–13128 (1989).

[39]In principle, existing classical force fields can also be used for a fast calculation of the Θ_p tensors, as the definition of the latter is not specific of the energy functional employed.

[40]K. Esfarjani and H. T. Stokes, "Method to extract anharmonic force constants from first principles calculations," Phys. Rev. B **77**, 144112 (2008).

[41]D. A. Case, "Normal mode analysis of protein dynamics," Curr. Opin. Struct. Biol. **4**, 285–290 (1994).

[42]L. Monacelli, R. Bianco, M. Cherubini, M. Calandra, I. Errea, and F. Mauri, "The stochastic self-consistent harmonic approximation: Calculating vibrational properties of materials with full quantum and anharmonic effects," J. Phys.: Condens. Matter **33**, 363001 (2021).

[43]J. M. Ziman, *Electrons and Phonons: The Theory of Transport Phenomena in Solids* (Oxford University Press, United Kingdom, 2001).

[44]S. Nosé, "A molecular dynamics method for simulations in the canonical ensemble," Mol. Phys. **52**, 255–268 (1984).

[45]S. Nosé, "A unified formulation of the constant temperature molecular dynamics methods," J. Chem. Phys. **81**, 511–519 (1984).

[46]W. G. Hoover, "Canonical dynamics: Equilibrium phase-space distributions," Phys. Rev. A **31**, 1695–1697 (1985).

[47]Although the term *normal equations* is commonly used in the theory for solving least squares problems with a different meaning [C. L. Lawson and J. Richard, *Solving Least Squares Problems* (Society for Industrial and Applied Mathematics, 1974)], we can use it in this context without ambiguities.

[48]A. Cammarata, P. Nicolini, K. Simonovic, E. Ukraintsev, and T. Polcar, "Atomic-scale design of friction and energy dissipation," Phys. Rev. B **99**, 094309 (2019).

[49]A. Cammarata, "Phonon-phonon scattering selection rules and control: An application to nanofriction and thermal transport," RSC Adv. **9**, 37491–37496 (2019).

[50]A. Cammarata and T. Polcar, "Control of energy dissipation in sliding low-dimensional materials," Phys. Rev. B **102**, 085409 (2020).

[51]N. K. Ravichandran and D. Broido, "Phonon-phonon interactions in strongly bonded solids: Selection rules and higher-order processes," Phys. Rev. X **10**, 021063 (2020).

[52]Y. Xia, V. I. Hegde, K. Pal, X. Hua, D. Gaines, S. Patel, J. He, M. Aykol, and C. Wolverton, "High-throughput study of lattice thermal conductivity in binary rocksalt and zinc blende compounds including higher-order anharmonicity," Phys. Rev. X **10**, 041029 (2020).

[53]Y. Chen, J. Ma, S. Wen, and W. Li, "Body-centered-cubic structure and weak anharmonic phonon scattering in tungsten," Npj Comput. Mater. **5**, 98 (2019).

[54]"pindol," The software is available free of charge, 2024, https://github.com/acammarat/pindol, last accessed 07 March 2024.

[55]K. Esfarjani, G. Chen, and H. T. Stokes, "Heat transport in silicon from first-principles calculations," Phys. Rev. B **84**, 085204 (2011).

[56]J. Shiomi, K. Esfarjani, and G. Chen, "Thermal conductivity of half-Heusler compounds from first-principles calculations," Phys. Rev. B **84**, 104302 (2011).

[57]O. Hellman, I. A. Abrikosov, and S. I. Simak, "Lattice dynamics of anharmonic solids from first principles," Phys. Rev. B **84**, 180301 (2011).

[58]O. Hellman, P. Steneteg, I. A. Abrikosov, and S. I. Simak, "Temperature dependent effective potential method for accurate free energy calculations of solids," Phys. Rev. B **87**, 104111 (2013).

[59]O. Hellman and I. A. Abrikosov, "Temperature-dependent effective third-order interatomic force constants from first principles," Phys. Rev. B **88**, 144301 (2013).

[60]N. Shulumba, O. Hellman, and A. J. Minnich, "Lattice thermal conductivity of polyethylene molecular crystals from first-principles including nuclear quantum effects," Phys. Rev. Lett. **119**, 185901 (2017).

[61]A. Togo and I. Tanaka, "First principles phonon calculations in materials science," Scr. Mater. **108**, 1–5 (2015).

[62]A. Togo, L. Chaput, and I. Tanaka, "Distributions of phonon lifetimes in Brillouin zones," Phys. Rev. B **91**, 094306 (2015).

[63]F. Zhou, W. Nielson, Y. Xia, and V. Ozoliņš, "Lattice anharmonicity and thermal conductivity from compressive sensing of first-principles calculations," Phys. Rev. Lett. **113**, 185501 (2014).

[64]J. Brorsson, A. Hashemi, Z. Fan, E. Fransson, F. Eriksson, T. Ala-Nissila, A. V. Krasheninnikov, H.-P. Komsa, and P. Erhart, "Efficient calculation of the lattice thermal conductivity by atomistic simulations with ab initio accuracy," Adv. Theory Simul. **5**, 2100217 (2022).

[65]A. Togo and I. Tanaka, Spglib: A software library for crystal symmetry sea.

[66]X. Gonze, B. Amadon, P.-M. Anglade, J.-M. Beuken, F. Bottin, P. Boulanger, F. Bruneval, D. Caliste, R. Caracas, M. Côté, T. Deutsch, L. Genovese, P. Ghosez, M. Giantomassi, S. Goedecker, D. Hamann, P. Hermet, F. Jollet, G. Jomard, S. Leroux, M. Mancini, S. Mazevet, M. Oliveira, G. Onida, Y. Pouillon, T. Rangel, G.-M. Rignanese, D. Sangalli, R. Shaltaf, M. Torrent, M. Verstraete, G. Zerah, and J. Zwanziger, "ABINIT: First-principles approach to material and nanosystem properties," Comput. Phys. Commun. **180**, 2582–2615 (2009).

[67]X. Gonze, F. Jollet, F. Abreu Araujo, D. Adams, B. Amadon, T. Applencourt, C. Audouze, J.-M. Beuken, J. Bieder, A. Bokhanchuk, E. Bousquet, F. Bruneval, D. Caliste, M. Côté, F. Dahm, F. Da Pieve, M. Delaveau, M. Di Gennaro, B. Dorado, C. Espejo, G. Geneste, L. Genovese, A. Gerossier, M. Giantomassi, Y. Gillet, D. Hamann, L. He, G. Jomard, J. Laflamme Janssen, S. Le Roux, A. Levitt, A. Lherbier, F. Liu, I. Lukačević, A. Martin, C. Martins, M. Oliveira, S. Poncé, Y. Pouillon, T. Rangel, G.-M. Rignanese, A. Romero, B. Rousseau, O. Rubel, A. Shukri, M. Stankovski, M. Torrent, M. Van Setten, B. Van Troeye, M. Verstraete, D. Waroquiers, J. Wiktor, B. Xu, A. Zhou, and J. Zwanziger, "Recent developments in the ABINIT software package," Comput. Phys. Commun. **205**, 106–131 (2016).

[68]X. Gonze, "A brief introduction to the ABINIT software package," Z. Kristallogr.—Cryst. Mater. **220**, 558–562 (2005).

[69]N. Troullier and J. L. Martins, "Efficient pseudopotentials for plane-wave calculations," Phys. Rev. B **43**, 1993–2006 (1991).

[70]L. Kleinman and D. M. Bylander, "Efficacious form for model pseudopotentials," Phys. Rev. Lett. **48**, 1425–1428 (1982).

[71] S. Goedecker, M. Teter, and J. Hutter, "Separable dual-space Gaussian pseudopotentials," Phys. Rev. B **54**, 1703–1710 (1996).

[72] H. J. Monkhorst and J. D. Pack, "Special points for Brillouin-zone integrations," Phys. Rev. B **13**, 5188–5192 (1976).

[73] Regardless the number of associated symmetry operations, any q-point can be excluded from the anharmonic processes by the selection rules; in that case, it would contribute to the dynamics only with the corresponding kinetic and harmonic term of the potential energy.

[74] G. H. Lander, E. S. Fisher, and S. Bader, "The solid-state properties of uranium A historical perspective and review," Adv. Phys. **43**, 1–111 (1994).

[75] W. P. Crummett, H. G. Smith, R. M. Nicklow, and N. Wakabayashi, "Lattice dynamics of α-uranium," Phys. Rev. B **19**, 6028–6037 (1979).

[76] H. G. Smith, N. Wakabayashi, W. P. Crummett, R. M. Nicklow, G. H. Lander, and E. S. Fisher, "Observation of a charge-density wave in α-U at low temperature," Phys. Rev. Lett. **44**, 1612–1615 (1980).

[77] J. Bouchet, "Lattice dynamics of α uranium," Phys. Rev. B **77**, 024113 (2008).

[78] L. T. Lloyd, "Thermal expansion of alpha-uranium single crystals," J. Nucl. Mater. **3**, 67–71 (1961).

[79] L. T. Lloyd and C. Barrett, "Thermal expansion of alpha uranium," J. Nucl. Mater. **18**, 55–59 (1966).

[80] C. S. Barrett, M. H. Mueller, and R. L. Hitterman, "Crystal structure variations in alpha uranium at low temperatures," Phys. Rev. **129**, 625–629 (1963).

[81] T. Le Bihan, S. Heathman, M. Idiri, G. H. Lander, J. M. Wills, A. C. Lawson, and A. Lindbaum, "Structural behavior of α-uranium with pressures to 100 GPa," Phys. Rev. B **67**, 134102 (2003).

[82] J. Bouchet and F. Bottin, "Thermal evolution of vibrational properties of α-U," Phys. Rev. B **92**, 174108 (2015).

[83] G. Kresse and J. Hafner, "*Ab initio* molecular dynamics for liquid metals," Phys. Rev. B **47**, 558–561 (1993).

[84] G. Kresse and J. Hafner, "*Ab initio* molecular-dynamics simulation of the liquid-metal–amorphous-semiconductor transition in germanium," Phys. Rev. B **49**, 14251–14269 (1994).

[85] G. Kresse and J. Furthmüller, "Efficiency of ab-initio total energy calculations for metals and semiconductors using a plane-wave basis set," Comput. Mater. Sci. **6**, 15–50 (1996).

[86] G. Kresse and J. Furthmüller, "Efficient iterative schemes for *ab initio* total-energy calculations using a plane-wave basis set," Phys. Rev. B **54**, 11169–11186 (1996).

[87] G. Kresse and D. Joubert, "From ultrasoft pseudopotentials to the projector augmented-wave method," Phys. Rev. B **59**, 1758–1775 (1999).

[88] M. I. Aroyo, D. Orobengoa, G. de la Flor, E. S. Tasci, J. M. Perez-Mato, and H. Wondratschek, "Brillouin-zone database on the *Bilbao Crystallographic Server*," Acta Crystallogr., Sect. A: Found. Adv. **70**, 126–137 (2014).

[89] E. S. Tasci, G. de la Flor, D. Orobengoa, C. Capillas, J. M. Perez-Mato, and M. I. Aroyo, "An introduction to the tools hosted in the Bilbao Crystallographic Server," EPJ Web Conf. **22**, 00009 (2012).

[90] H. Tian, J. Tice, R. Fei, V. Tran, X. Yan, L. Yang, and H. Wang, "Low-symmetry two-dimensional materials for electronic and photonic applications," Nano Today **11**, 763 (2016).

[91] A. B. Kaul, "Two-dimensional layered materials: Structure, properties, and prospects for device applications," J. Mater. Res. **29**, 348 (2014).

[92] H. Li, J. Wu, Z. Yin, and H. Zhang, "Preparation and applications of mechanically exfoliated single-layer and multilayer MoS_2 and WSe_2 nanosheets," Acc. Chem. Res. **47**, 1067 (2014).

[93] M. Chhowalla, H. S. Shin, G. Eda, L.-J. Li, K. P. Loh, and H. Zhang, "The chemistry of two-dimensional layered transition metal dichalcogenide nanosheets," Nat. Chem. **5**, 263 (2013).

[94] A. K. Geim and I. V. Grigorieva, "Van der Waals heterostructures," Nature **499**, 419 (2013).

[95] A. Vanossi, N. Manini, M. Urbakh, S. Zapperi, and E. Tosatti, "*Colloquium*: Modeling friction: From nanoscale to mesoscale," Rev. Mod. Phys. **85**, 529 (2013).

[96] H. G. Füchtbauer, A. K. Tuxen, P. G. Moses, H. Topsøe, F. Besenbacher, and J. V. Lauritsen, "Morphology and atomic-scale structure of single-layer WS_2 nanoclusters," Phys. Chem. Chem. Phys. **15**, 15971 (2013).

[97] S. Helveg, J. V. Lauritsen, E. Lægsgaard, I. Stensgaard, J. K. Nørskov, B. S. Clausen, H. Topsøe, and F. Besenbacher, "Atomic-scale structure of single-layer MoS_2 nanoclusters," Phys. Rev. Lett. **84**, 951 (2000).

[98] R. Saito, Y. Tatsumi, S. Huang, X. Ling, and M. S. Dresselhaus, "Raman spectroscopy of transition metal dichalcogenides," J. Phys.: Condens. Matter **28**, 353002 (2016).

[99] D. C. Harris and M. D. Bertolucci, in *Symmetry and Spectroscopy, Dover Books on Chemistry* (Dover Publications, Mineola, NY, 1989).

[100] P. Atkins, J. De Paula, and R. S. Friedman, *Physical Chemistry*, 2nd ed. (Oxford University Press, London, England, 2013).

[101] S. Najmaei, Z. Liu, P. M. Ajayan, and J. Lou, "Thermal effects on the characteristic Raman spectrum of molybdenum disulfide (MoS_2) of varying thicknesses," Appl. Phys. Lett. **100**, 013106 (2012).

[102] N. A. Lanzillo, A. Glen Birdwell, M. Amani, F. J. Crowne, P. B. Shah, S. Najmaei, Z. Liu, P. M. Ajayan, J. Lou, M. Dubey, S. K. Nayak, and T. P. O'Regan, "Temperature-dependent phonon shifts in monolayer MoS_2," Appl. Phys. Lett. **103**, 093102 (2013).

[103] S. Mignuzzi, A. J. Pollard, N. Bonini, B. Brennan, I. S. Gilmore, M. A. Pimenta, D. Richards, and D. Roy, "Effect of disorder on Raman scattering of single-layer MoS_2," Phys. Rev. B **91**, 195411 (2015).

[104] H. Guo, Y. Sun, P. Zhai, H. Yao, J. Zeng, S. Zhang, J. Duan, M. Hou, M. Khan, and J. Liu, "Swift-heavy ion irradiation-induced latent tracks in few- and mono-layer MoS_2," Appl. Phys. A **122**, 375 (2016).

[105] S. Sahoo, A. P. S. Gaur, M. Ahmadi, M. J.-F. Guinel, and R. S. Katiyar, "Temperature-dependent Raman studies and thermal conductivity of few-layer MoS_2," J. Phys. Chem. C **117**, 9042–9047 (2013).

[106] G. P. Srivastava and I. O. Thomas, "Temperature-dependent Raman linewidths in transition-metal dichalcogenides," Phys. Rev. B **98**, 035430 (2018).

[107] Z. Hu, Y. Bao, Z. Li, Y. Gong, R. Feng, Y. Xiao, X. Wu, Z. Zhang, X. Zhu, P. M. Ajayan, and Z. Fang, "Temperature dependent Raman and photoluminescence of vertical WS_2/MoS_2 monolayer heterostructures," Sci. Bull. **62**, 16–21 (2017).

[108] M. Öper, Y. Shehu, and N. K. Perkgöz, "Temperature-dependent Raman modes of $MoS_2/MoSe_2$ van der Waals heterostructures," Semicond. Sci. Technol. **35**, 115020 (2020).

[109] B. Schönfeld, J. J. Huang, and S. C. Moss, "Anisotropic mean-square displacements (MSD) in single-crystals of 2H- and 3R-MoS_2," Acta Crystallogr., Sect. B: Struct. Sci. **39**, 404–407 (1983).

[110] Z. Zhao, H. Zhang, H. Yuan, S. Wang, Y. Lin, Q. Zeng, G. Xu, Z. Liu, G. K. Solanki, K. D. Patel, Y. Cui, H. Y. Hwang, and W. L. Mao, "Pressure induced metallization with absence of structural transition in layered molybdenum diselenide," Nat. Commun. **6**, 7312 (2015).

[111] W. Schutte, J. De Boer, and F. Jellinek, "Crystal structures of tungsten disulfide and diselenide," J. Solid State Chem. **70**, 207–209 (1987).

[112] F. Belviso, A. Cammarata, J. Missaoui, and T. Polcar, "Effect of electric fields in low-dimensional materials: Nanofrictional response as a case study," Phys. Rev. B **102**, 155433 (2020).

[113] A. D. Becke and E. R. Johnson, "A simple effective potential for exchange," J. Chem. Phys. **124**, 221101 (2006).

[114] Phonopy-spectroscopy, https://github.com/JMSkelton/Phonopy-Spectroscopy, last accessed 05 March 2023.

[115] J. M. Skelton, L. A. Burton, A. J. Jackson, F. Oba, S. C. Parker, and A. Walsh, "Lattice dynamics of the tin sulphides SnS_2, SnS and Sn_2S_3: Vibrational spectra and thermal transport," Phys. Chem. Chem. Phys. **19**, 12452–12465 (2017).

[116] ascii-phonons, https://github.com/ajjackson/ascii-phonons, last accessed 05 March 2023.

[117] V_Sim, https://www.mem-lab.fr/en/Pages/L_SIM/Softwares/V_Sim.aspx, last accessed 05 March 2023.

[118] eigmap, 2023, https://github.com/acammarat/phtools/tree/main/eigmap, last accessed 17 March 2023.

[119] A. Cammarata and T. Polcar, "Fine control of lattice thermal conductivity in low-dimensional materials," Phys. Rev. B **103**, 035406 (2021).

[120] A. Del Monte, N. Manini, L. Guido Molinari, and G. Paolo Brivio, "Low-energy unphysical saddle in polynomial molecular potentials," Mol. Phys. **103**, 689–696 (2005).

[121] I. Mills and A. Robiette, "On the relationship of normal modes to local modes in molecular vibrations," Mol. Phys. **56**, 743–765 (1985).

[122] K. A. Dill, "Polymer principles and protein folding," Protein Sci. **8**, 1166–1180 (1999).

[123] M. Simoncelli, N. Marzari, and F. Mauri, "Wigner formulation of thermal transport in solids," Phys. Rev. X **12**, 041011 (2022).

[124] T. Luo and G. Chen, "Nanoscale heat transfer—From computation to experiment," Phys. Chem. Chem. Phys. **15**, 3389–3412 (2013).

[125] Y. Luo, X. Yang, T. Feng, J. Wang, and X. Ruan, "Vibrational hierarchy leads to dual-phonon transport in low thermal conductivity crystals," Nat. Commun. **11**, 2554 (2020).

[126] C. Yang, X. Wei, J. Sheng, and H. Wu, "Phonon heat transport in cavity-mediated optomechanical nanoresonators," Nat. Commun. **11**, 4656 (2020).

[127] S. Lee, D. Broido, K. Esfarjani, and G. Chen, "Hydrodynamic phonon transport in suspended graphene," Nat. Commun. **6**, 6290 (2015).

[128] H. S. Yoon, J. Oh, J. Y. Park, J. Kang, J. Kwon, T. Cusati, G. Fiori, G. Iannaccone, A. Fortunelli, V. O. Ozcelik, G.-H. Lee, T. Low, and S. C. Jun, "Phonon-assisted carrier transport through a lattice-mismatched interface," npg Asia Mater. **11**, 14 (2019).

[129] L. Lindsay, A. Katre, A. Cepellotti, and N. Mingo, "Perspective on *ab initio* phonon thermal transport," J. Appl. Phys. **126**, 050902 (2019).

[130] J.-M. Manceau, P. A. Loukakos, and S. Tzortzakis, "Direct acoustic phonon excitation by intense and ultrashort terahertz pulses," Appl. Phys. Lett. **97**, 251904 (2010).

[131] Y. Wang, L. Guo, X. Xu, J. Pierce, and R. Venkatasubramanian, "Origin of coherent phonons in Bi_2Te_3 excited by ultrafast laser pulses," Phys. Rev. B **88**, 064307 (2013).

[132] J. D. Schall, P. T. Mikulski, G. M. Chateauneuf, G. Gao, and J. A. Harrison, "5—Molecular dynamics simulations of tribology," in *Superlubricity*, edited by A. Erdemir and J.-M. Martin (Elsevier Science B.V., Amsterdam, 2007), pp. 79–102.

[133] A. I. Vakis, V. A. Yastrebov, J. Scheibert, L. Nicola, D. Dini, C. Minfray, A. Almqvist, M. Paggi, S. Lee, G. Limbert, J. F. Molinari, G. Anciaux, R. Aghababaei, S. Echeverri Restrepo, A. Papangelo, A. Cammarata, P. Nicolini, C. Putignano, G. Carbone, S. Stupkiewicz, J. Lengiewicz, G. Costagliola, F. Bosia, R. Guarino, N. M. Pugno, M. H. Müser, and M. Ciavarella, "Modeling and simulation in tribology across scales: An overview," Tribol. Int. **125**, 169–199 (2018).

[134] J. Lu and E. Vanden-Eijnden, "Infinite swapping replica exchange molecular dynamics leads to a simple simulation patch using mixture potentials," J. Chem. Phys. **138**, 084105 (2013).

[135] A. Jain, S. P. Ong, G. Hautier, W. Chen, W. D. Richards, S. Dacek, S. Cholia, D. Gunter, D. Skinner, G. Ceder, and K. a. Persson, "Commentary: The materials project: A materials genome approach to accelerating materials innovation," APL Mater. **1**, 011002 (2013).

[136] S. P. Huber, S. Zoupanos, M. Uhrin, L. Talirz, L. Kahle, R. Häuselmann, D. Gresch, T. Müller, A. V. Yakutovich, C. W. Andersen, F. F. Ramirez, C. S. Adorf, F. Gargiulo, S. Kumbhar, E. Passaro, C. Johnston, A. Merkys, A. Cepellotti, N. Mounet, N. Marzari, B. Kozinsky, and G. Pizzi, "AiiDA 1.0, a scalable computational infrastructure for automated reproducible workflows and data provenance," Sci. Data **7**, 300 (2020).

[137] F. Belviso, V. E. P. Claerbout, A. Comas-Vives, N. S. Dalal, F.-R. Fan, A. Filippetti, V. Fiorentini, L. Foppa, C. Franchini, B. Geisler, L. M. Ghiringhelli, A. Groß, S. Hu, J. Íñiguez, S. K. Kauwe, J. L. Musfeldt, P. Nicolini, R. Pentcheva, T. Polcar, W. Ren, F. Ricci, F. Ricci, H. S. Sen, J. M. Skelton, T. D. Sparks, A. Stroppa, A. Urru, M. Vandichel, P. Vavassori, H. Wu, K. Yang, H. J. Zhao, D. Puggioni, R. Cortese, and A. Cammarata, "Viewpoint: Atomic-Scale design protocols toward energy, electronic, catalysis, and sensing applications," Inorg. Chem. **58**, 14939–14980 (2019).